at a rate of 4.8 protons $cm^{-2}$ $s^{-1}$—that is, the GCR primary particle spectrum averaged over a typical solar cycle. The production rate of $^{59}$Ni was calculated by integration over the energy of the product of neutron fluxes, computed by LCS, and neutron-capture cross sections weighted by target nuclei concentration. Statistical uncertainties of 2 to 3% are associated with the numbers of particles simulated; overall uncertainties of ~15% allow for the uncertainties of the cross sections and primary GCR flux. The calculations depend weakly on radius in this size region and should describe, within the uncertainties, $^{59}$Ni production in bodies with radii from 13 to 17 m (*23*) [J. Masarik and R. C. Reedy, *Geochim. Cosmochim. Acta* **58**, 5307 (1994); R. E. Prael and H. Lichtenstein, *Los Alamos Report LA-UR-89-3014I* (1989); J. F. Briesmeister, *Los Alamos Report LA-12625-M* (1993)].

13. The activity of terrestrially produced $^{59}$Ni, $A_{59}$, in the spheroids is calculated to be 0.15 disintegrations per minute per kilogram from the relation

$$A_{59} = [1 - \exp(-\lambda_{59} t_{\text{terrestrial}})] \times {}^{58}Ni \int_{1 \times 10^{-8}\ \text{MeV}}^{20\ \text{MeV}} \Phi(E)\sigma(E)dE$$

where $^{58}Ni$ is the concentration of that isotope; $\Phi(E)$ is the flux of neutrons at energy $E$ calculated by LCS (*12*) at the elevation of Meteor Crater, 1561 m (J. Masarik and J. Beer, *J. Geophys. Res.* **B104**, 12099 (1999); $\sigma(E)$ is the cross section for neutron capture by $^{58}$Ni (*23*); $\lambda_{59}$ is the decay constant for $^{59}$Ni, $1.73 \times 10^{-11}$ $min^{-1}$; the concentration of $^{58}$Ni is based on an average total Ni content of ~16% in spheroids (*6*); and $t_{\text{terrestrial}}$ is the time of impact of the Canyon Diablo meteoroid, 0.05 million years ago (*1*).

14. A value of 15 km $s^{-1}$ corresponds to the median impact speed and a value of 20 km $s^{-1}$ to the average impact speed for known Earth-crossing asteroids [C. F. Chyba, *Icarus* **92**, 217 (1991); ———, T. C. Owen, W.-H. Ip, in *Hazards Due to Comets and Asteroids*, T. Gerhels, Ed. (Univ. of Arizona Press, Tucson, 1994), pp. 9–58; D. L. Rabinowitz, E. Bowell, E. M. Shoemaker, K. Muinonen, *ibid*., pp. 285–312].
15. S. L. Thompson, *Tech. Rep. SAND77-1339* (Sandia National Laboratory, Albuquerque, NM, 1979).
16. ——— and H. S. Lauson, *Tech. Rep. SC-RR-710714* (Sandia National Laboratory, Albuquerque, NM, 1972).
17. E. Pierazzo, A. M. Vickery, H. J. Melosh, *Icarus* **127**, 408 (1997).
18. H. J. Melosh, *Impact Cratering* (Oxford, New York, 1989).
19. J. D. Bass, B. Svendsen, T. J. Ahrens, in *High-Pressure Research in Mineral Physics,* M. H. Manghnani and Y. Syono, Eds. (Terra Scientific, Tokyo/American Geophysical Union, Washington, DC, 1987), pp. 393–402.
20. J. D. Bass, T. J. Ahrens, J. R. Abelson, T. Hua, *J. Geophys. Res.* **95**, 21767 (1990).
21. The process of target decompression but not of meteoroid dispersal is described by S. W. Kieffer and C. H. Simonds [*Rev. Geophys. Space Phys.* **18**, 143 (1980)].
22. E. Pierazzo, D. A. Kring, H. J. Melosh, *J. Geophys. Res.* **103**, 28607 (1998); E. Pierazzo and H. J. Melosh, *Earth Planet. Sci. Lett.* **165**, 163 (1999).
23. Cross Section Evaluation Working Group, *Report BNL-NCS-44945* (*ENDF-102*) (Brookhaven National Laboratory, Upton, NY 1995).
24. J. Klein *et al*., *Lunar Planet. Sci.* **XXVI**, 763 (1995).
25. To place all the Canyon Diablo $^{59}$Ni contents, whether measured in meteorites or in spheroids, on a consistent scale, we converted $^{59}$Ni/Ni ratios to $^{59}$Ni activities in an object with the average Ni content, 7.1 weight %, of Canyon Diablo meteorites [C. B. Moore, J. Littler, D. Nava, in *Meteorite Research,* P. M. Millman, Ed. (Springer-Verlag, New York, 1969), pp. 738–748; B. Mason and E. Jarosewich, *Mineral. Mag.* **39**, 204 (1973)]. This Ni content was also used in the nuclear modeling calculations. In addition, iron and nickel contents were measured by direct current atomic emission spectrometry (DC-AES) and inductively coupled plasma mass spectrometry (ICP-MS), respectively, yielding the following values (weight %): MPIH-3: Fe 92.3, Ni 6.6; MPIH-266: Fe 92.5, Ni 6.2; 34.4340: Fe 93.8, Ni 6.6; 34.4367: Fe 91.8, Ni 6.5; III-3: Fe 75.1, Ni 14.0; IV-3: Fe 82.1, Ni 14.1; V-3: Fe 78.3, Ni 18.4. Relative uncertainties are 5% for both elements.
26. M. Honda and J. R. Arnold, *Handb. Phys.* **46**, 613 (1967).
27. J. H. Kaye, in *Nuclear Chemistry Research at Carnegie Institute of Technology, 1961–1962* [Progress Report for U.S. Atomic Energy Commission Contract AT(30-1)-844, 1962], pp. 43–46.
28. The nuclear modeling calculations extend only to a depth of 2 m. Wiggles in the curve reflect statistical limitations set by the number of particles followed through the calculation. We used a polynomial fit to extrapolate the production rates to depths greater than 2 m. The data points have been placed on the curve at the depths inferred from the modeling calculations.
29. We thank R. Clarke Jr. for sample N3311; T. Kirsten for Canyon Diablo samples MPIH-3 and MPIH-266; M. E. Lipschutz for Canyon Diablo samples 34.4340 and 34.4367; C. Moore for spheroids; and J. Klein, A. Hildebrand, and two anonymous referees for helpful contributions to this work. Supported in part by NASA grants NAG5-4327 and NAGW-5159 and U.S. Department of Energy contract DE-FG03-96ER14676.

1 March 1999; accepted 3 June 1999

# Atomic-Scale Quasi-Particle Scattering Resonances in $Bi_2Sr_2CaCu_2O_{8+\delta}$

**E. W. Hudson,[1] S. H. Pan,[1]* A. K. Gupta,[2] K.-W. Ng,[2] J. C. Davis[1]†**

**Low-temperature scanning tunneling spectroscopy of the high transition temperature (high-$T_c$) cuprate $Bi_2Sr_2CaCu_2O_{8+\delta}$ reveals the existence of large numbers of identical regions with diameters of about 3 nanometers that have a relatively high density of low-energy quasi-particle states. Their spatial and spectroscopic characteristics are consistent with theories of strong quasi-particle scattering from atomic-scale impurities in a *d*-wave superconductor. These characteristics include breaking of local particle-hole symmetry, a diameter near twice the superconducting coherence length, and an inverse square dependence of their local density-of-states on distance from the scattering center. In addition to the validation of *d*-wave quasi-particle scattering theories, these observations identify a source for the anomalously high levels of low-energy quasi-particles in $Bi_2Sr_2CaCu_2O_{8+\delta}$ at low temperatures.**

Impurity atoms and atomic-scale defects, even in very small concentrations, can strongly influence the properties of materials. This is of great practical significance in semiconductor technology, for example, where the conductivity of pure semiconductors can be increased many orders of magnitude by doping with a few parts per million of specific impurities. Another example is the doping of small numbers of Ti atoms into sapphire to create the optical conditions necessary for high-power, tunable lasers.

Impurities also play a critical role in superconductivity. Conventional superconductors, such as Nb and Pb, are highly sensitive to the presence of magnetic impurity atoms (*1*), which suppress the critical temperature by breaking Cooper pairs through spin-flip scattering (*2*). Nonmagnetic impurities, on the other hand, have little effect on conventional superconductors. In the high-$T_c$ superconductors, however, doping even with nonmagnetic impurities can cause dramatic effects. In fact, it is hole doping in the form of additional oxygen atoms that turns the cuprate oxides from antiferromagnetic insulators into high-$T_c$ superconductors. However, impurity doping with Zn or Ni is known to reduce the critical temperature, modify the energy gap, increase the residual resistivity, and alter the vortex phase diagram (*3–5*).

Despite many important effects of impurity atoms on the macroscopic properties of high-$T_c$ superconductors (*6*) and despite numerous proposals for scanning tunneling microscopy (STM) study of impurity quasi-particle scattering in these systems (*7–11*), no direct observation and systematic study of the effects of quasi-particle scattering at the atomic scale have been reported. Theory indicates that quasi-particle scattering at impurities can reveal information about the symmetry of the order parameter, the momentum dependence of the energy gap, and the microscopic mechanism of superconductivity (*8, 12*). Several studies predict that impurity atoms create quasi-particle scattering resonances that have characteristic signatures both in the spatial shape of the quasi-particle cloud near the scattering center and in their tunneling spectrum (*7–12*). Furthermore, it has also been

[1]Department of Physics, University of California, Berkeley, CA, 94720–7300, USA. [2]Department of Physics and Astronomy, University of Kentucky, Lexington, KY 40506–0055, USA.

*Present address: Department of Physics, Boston University, Boston, MA, 02215, USA.

†To whom correspondence should be addressed. E-mail: jcdavis@socrates.berkeley.edu

predicted that the low-energy quasi-particle states generated by quasi-particle scattering may be crucial to understanding well-known but unexplained low-temperature anomalies in the transport properties (*13–17*).

Impurity scattering in a conventional superconductor has been investigated by Yazdani *et al.* (*18*). These workers used STM to study quasi-particle scattering from both magnetic and nonmagnetic adatoms that were deposited on the surface of a Nb crystal. For nonmagnetic atoms, no effect was observed in the local density of states near the impurity, whereas for magnetic impurities (Mn and Gd), a characteristic quasi-particle scattering spectrum was observed. Tunneling spectroscopy over a single oxygen vacancy site in the CuO-chain plane of $YBa_2Cu_3O_{7-\delta}$ has also been reported by de Lozanne and co-workers (*19*).

We report direct observation and systematic study of atomic-scale quasi-particle scattering in single-crystal $Bi_2Sr_2CaCu_2O_{8+\delta}$ (BSCCO). For these studies, we used a high-resolution STM (*20*) operated at 4.2 K. The utility of the STM lies in its ability to simultaneously measure, with atomic resolution, both the surface topography and the local density of states (LDOS) of a material. This ability is derived from the exponential dependence of the tunneling current $I$ on the tip/sample separation, and the proportionality of the differential conductance $G = dI/dV$ (where $V$ is the sample bias voltage) to the LDOS of the sample at the tip location (*21*). Because the coherence length of the high-$T_c$ superconductors is only a few nanometers, a high spatial resolution STM is a necessity when attempting to identify the location and geometry of scattering sites and study their atomic-scale effects on the quasi-particle density of states.

The STM tips used in these studies, either PtIr or W, were cleaned and sharpened in cryogenic ultrahigh vacuum at 4.2 K by field emission against an Au target (*22*). The samples, BSCCO single crystals grown by the directional solidification method (*23*) and measured to have a $T_c$ of 87 K with a transition width of 5 K, were cleaved at 4.2 K and immediately inserted into the STM head. A high-resolution topographic scan was taken to determine the condition of the crystal surface (Fig. 1). Although we occasionally observed terraces of different atomic layers (*24*), BSCCO most often cleaves to reveal a single BiO layer with only the Bi atoms apparent in STM topography (*25*). The atoms are observed to be displaced from their ideal orthorhombic lattice sites, forming a well-known supermodulation with wave vector along the *b*-axis (*26*). A sinusoidal pattern, which appears to be due to missing atoms in the surface (*25*), was observed at each crest of the modulation.

Following atomic resolution imaging of a larger area, we mapped the differential conductance at zero bias on the same area. Such a map is a measure of the LDOS of low-energy quasi-particles and, in a superconductor at temperatures far below $T_c$, is expected to show a uniform very low differential conductance. In the color scale used here, this would appear uniformly dark. In contrast to this expectation, a typical zero-bias conductance map in BSCCO (Fig. 2) revealed a large number of localized bright features which have a relatively high LDOS near the Fermi energy $E_f$. These features are of similar size and shape, with a diameter $d = 3.1 \pm 0.2$ nm, and appear to be randomly distributed (although they are clustered at some locations). Approximately 150 of these features are observed in this 130-nm field of view. The same average density of these features was observed in multiple samples. For reasons to be outlined below, we attribute these LDOS features to quasi-particle scattering from atomic-scale defects or impurities, resulting in a resonance of the virtual impurity-bound states (*8*). We refer to these features as quasi-particle scattering resonances (QPSRs).

Because of its fundamental importance as an atomic-scale probe of the superconducting order parameter, many workers have studied theoretically the effects of quasi-particle scattering from atomic-scale impurities or defects in a *d*-wave superconductor. Predictions for the characteristics of a QPSR at an atomic-scale scatterer in a *d*-wave superconductor include the LDOS spectrum as a function of impurity scattering strength (*8, 10*), the dependence of the LDOS on distance from the scattering center (*6, 8–10*), the size of a QPSR in terms of the superconducting coherence length, and the spatial shape of the LDOS near a QPSR (*6–8, 12, 15*).

For comparison with these predictions, we carried out a series of spectroscopic measurements on a number of QPSRs. We note that when QPSRs are close together, the tunneling spectra are observed to be quite complicated, as has been predicted (*6*). In an attempt to identify their representative properties, we selected for further study several QPSRs that have no others within at least 8 nm. A typical tunneling spectrum measured at the center of such a QPSR (Fig. 3A, solid line) is compared with that taken on a "good" (exhibiting no impurity scattering) superconducting area of the crystal (dashed line). Aside from the slight suppression of the coherent quasi-particle peaks at the edge of the superconducting gap, the most significant difference between these two curves is a peak in the tunneling conductance spectrum at energies near the Fermi level. Investigation of large numbers of QPSRs show that this peak occurs at varying energies $\Omega_0$, but always just below $E_f$, and its magnitude increases with increasing $|\Omega_0|$, as has been predicted (*8*). On average, the spectrum of a QPSR in the crystals studied has $\Omega_0 = -1.3 \pm 0.4$ meV, with a width (full width at half maximum) of 4 meV and an amplitude of 20 to 30% of the normal state conductance.

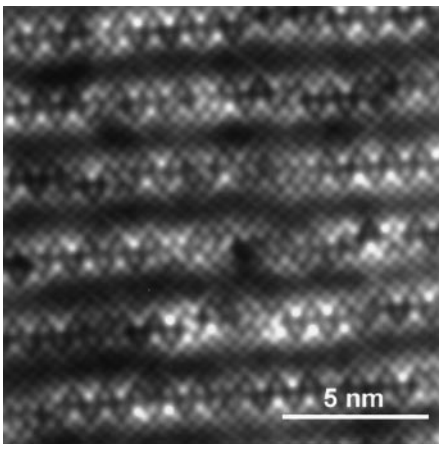


**Fig. 1.** Typical constant current topograph (15-nm square), showing both atomic resolution and the supermodulation. Imaged at $T = 4.2$ K, $I = 100$ pA, $V_{sample} = -100$ mV.

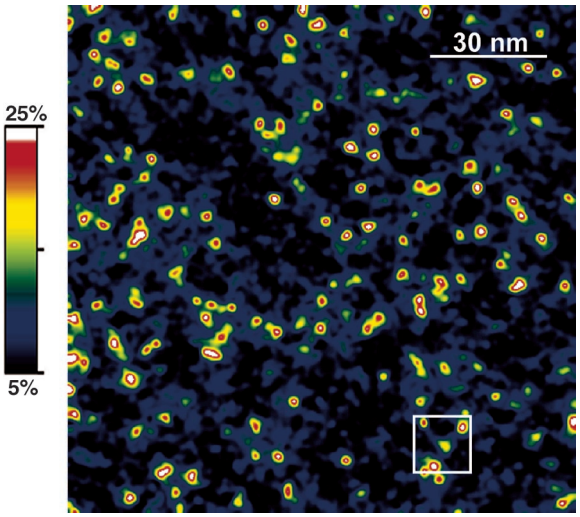


**Fig. 2.** A 130-nm square zero-bias conductance map. The QPSRs appear as bright regions ~3 nm in diameter, owing to their higher zero-bias conductance. The color scale, in terms of percentage of normal state conductance, is shown at left. This entire area is resolved with atomic resolution in topography. Because reproduction techniques do not have enough dynamic range to simultaneously show atomic resolution and ~100-nm-scale field of view, we only show as an example (Fig. 1) the area marked by a white frame. For the differential conductance map, we set a 1-gigohm junction resistance (100 pA, –100 mV) and measured the conductance with a lock-in technique ($A_{modulation} = 500\ \mu V_{rms}$, $f = 447.3$ Hz).

A number of theoretical studies have predicted the breaking of particle-hole symmetry as a property of quasi-particle scattering from a strong scattering center in a *d*-wave superconductor (*8–12*). For example, Salkola, Balatsky, and Scalapino (*8*) (SBS) recently proposed a model of quasi-particle scattering from a center described by a δ-function potential: $U(r) = U\delta(r)$. With a T-matrix formulation, they find that the virtual bound-state resonance will occur at an energy given by

$$\Omega_0 \approx \Delta_0(2U\ln|8U|)^{-1} \quad (1)$$

where $\Delta_0$ is the superconducting energy gap magnitude, and $U$ is the scattering strength in units of the inverse of the density of states at the Fermi energy $N_F$.

Analysis of our observations in terms of this model indicates that the scattering potential is attractive ($U < 0$), as the resonances are observed below the Fermi level. The high-resolution tunneling conductance spectrum of a QPSR (Fig. 3B) is obtained by averaging the spectra of six well-isolated QPSRs and subtracting a typical conductance spectrum of a "good" area in order to extract only the contribution from the scattering resonance.

Using the value $\Omega_0 = -1.3$ meV (from our data, solid circles in Fig. 3B) and $\Delta_0 = 32$ meV (*27*), we can invert Eq. 1 to give $U = -3.6\ N_F^{-1}$. By substituting these values into the SBS model, the predicted LDOS of a QPSR can be obtained. From this LDOS and the thermally broadened LDOS of the normal-state tip, we then derive an expected tunneling conducance spectrum of the QPSR (Fig. 3B, dashed line) and find it to be in reasonable agreement with the measured QPSR conductance spectrum.

The QPSRs also have a very similar physical extent to that predicted (*7, 8*), with observed diameters near 3 nm. Theory indicates a diameter of about two coherence lengths $\xi_0$, and in BSCCO, $\xi_0$ is measured to be 1.5 nm (*28*). Furthermore, the dependence of the LDOS of a QPSR on distance $r$ from its center can be analyzed by plotting the tunneling conductance $G$ as a function of $r$ on a log-log scale (Fig. 4). To extract this data, we first averaged the LDOS maps of five different, well-isolated, QPSRs which were scanned with high spatial resolution, and then averaged the result over azimuthal angles. A linear fit to the data (shown as a solid line), beginning at a distance of $\xi_0$ from the QPSR center, gives a slope of $-1.97 \pm 0.07$. This result is in excellent agreement with predictions (*6, 8*) that $G(r) \propto 1/r^2$ for $r > \xi_0$.

In addition to theoretical predictions of the tunneling spectrum, physical extent, and $G(r)$ of the QPSRs, which are all in good agreement with our observations, a fourfold cross shape for the QPSR has also been predicted by several authors (*6–8*). This shape is expected because quasi-particles can escape from the scattering site along the directions of the four nodes in a $d_{x^2-y^2}$ gap. However, it has not been evident in our measurements. There are several possible explanations for its absence. First, the cross shape may not, in fact, exist in BSCCO because of strong coupling (*15*). Secondly, the QPSRs may not be separated by a large enough distance for this weak phenomenon to be obvious (*6*). Finally, the signal-to-noise ratio of our measurement may be insufficient in the regions distant from the center of a QPSR where the star shape might be observed.

Identification of the scattering centers causing the QPSRs will require further study. Possible candidates include: crystal defects, elemental impurities, and oxygen inhomogeneities. When the position of the QPSRs is analyzed for a correlation with the simultaneously acquired high-resolution topographic data, no strong correlation is found. Elemental impurities might be present in these crystals, but microprobe analysis of these samples shows that the concentration of impurities is below 0.05% by weight (which is the sensitivity limit of this technique) for Mg, Ni, Fe, Al, and Co. However, this does not rule out the possibility of elemental impurities, as the observed QPSR concentration is below this limit. We note that the absence of any effects on the QPSRs from magnetic fields up to 7.25 T supports the view that their source is nonmagnetic. Since oxygen inhomogeneity is universal in high-$T_c$ materials, the third possibility is intriguing. At present, we are unable to differentiate between these situations, but future experiments, with systematic oxygen concentration studies or deliberate doping of known impurities, should allow relation of the spectra to the identity of the scatterers.

Independent of the identification of the scattering centers, the observation of these QPSRs is significant in itself, because it validates several theories of the effects of scattering at the atomic scale in *d*-wave superconductors. In addition, it also yields a new understanding of other properties of BSCCO. Theories have long been proposed that impurity scattering–induced states might lead to a number of different transport properties (*6, 13–16*). Experimentally, both thermal conductivity (*29*) and high-frequency electrical conductivity (*30, 31*) measurements at low temperatures have provided evidence of excess low-energy quasi-particle states. This excess can be understood by considering the observed spatial extension of the QPSRs. At an arbitrary point in the crystal, the sum of the $1/r^2$ tails from all nearby QPSRs contributes to a finite low-energy density of

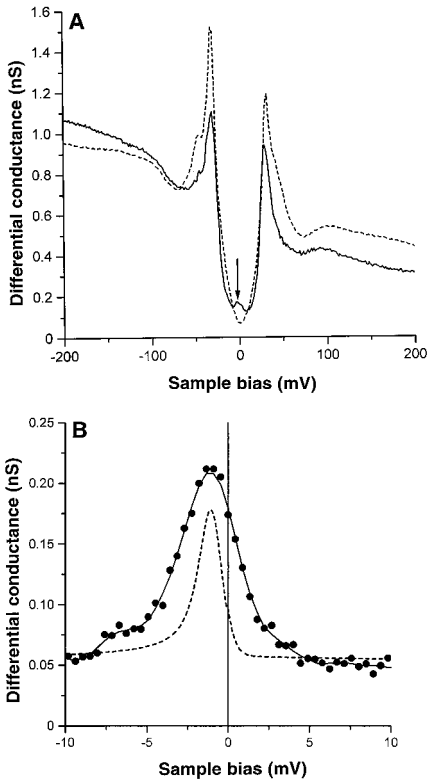


**Fig. 3.** (**A**) Tunneling conductance versus sample bias taken at two different locations on the BSCCO crystal. The dashed line is taken on a "good" superconducting region, where QPSRs are absent. The solid line is a typical spectrum taken at the center of a QPSR, exhibiting a low-energy resonance peak (indicated by the arrow). (**B**) The average of high-resolution spectra taken at the centers of six different QPSRs (solid circles). A typical "good" region spectrum has been subtracted to clarify the scattering contribution. The solid line is a guide to the eye. The theoretically predicted spectrum calculated using the SBS model, including the effects of thermal broadening in the tip spectrum at 4.2 K and the finite zero-bias density of states background, is shown as a dashed line.

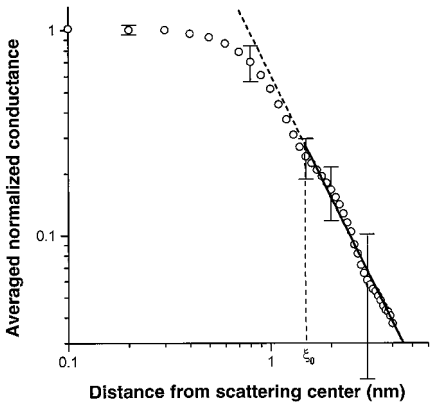


**Fig. 4.** Differential conductance $G$ at $V = -1$ mV versus distance $r$ from the center of a QPSR. The data (circles) are extracted from the average of normalized high-resolution conductance maps of five different isolated QPSRs. To calculate $G(r)$, an average is then taken over azimuthal angles. The solid line is a linear fit, starting at $\xi_0 = 1.5$ nm from the QPSR center, and gives a slope of $-1.97 \pm 0.07$, which is in excellent agreement with the predicted power law of $1/r^2$. The fit is extended as a dashed line to $r$ values below $\xi_0$ as a guide to the eye.

states. This can be seen, for example, as a finite zero-bias conductance in tunneling spectroscopy, and may be responsible for the excess quasi-particles identified in bulk measurements.

The above data give direct evidence of a strong source of low-energy quasi-particle excitations in BSCCO even at low temperatures. The observed QPSR characteristics, including breaking of particle-hole symmetry, diameter of $2\xi_0$, and LDOS decay as $1/r^2$, are all consistent with strong quasi-particle scattering from atomic-scale scatterers in a *d*-wave (but not *s*-wave) superconductor. Finally, this experiment demonstrates the possibility of using a single atomic-scale scatterer as a probe of high-$T_c$ superconductivity. This technique might eventually be used, with specific elemental impurities deliberately doped into different atomic planes, to help unlock the secrets of the mechanism of high-$T_c$ superconductivity.

*Note added in proof*: Since the submission of this manuscript, the authors have become aware of a recent study on atomic-scale impurities (*32*).

**References and Notes**


1. M. A. Woolf and F. Reif, *Phys. Rev.* **137**, A557 (1965).
2. A. A. Abrikosov and L. P. Gor'kov, *Zh. Eksp. Teor. Fiz.* **39**, 1781 (1960); *Sov. Phys. JETP* **12**, 1243 (1961).
3. H. Hancotte, R. Deltour, D. N. Davydov, A. G. M. Jansen, P. Wyder, *Phys. Rev. B* **55**, R3410 (1997).
4. R. Noetzel and K. Westerholt, *ibid.* **58**, 15108 (1998).
5. P. J. White *et al.*, http://xxx.lanl.gov/abs/cond-mat/9901349
6. A. V. Balatsky and M. I. Salkola, *Phys. Rev. Lett.* **76**, 2386 (1996), and references therein.
7. J. M. Byers, M. E. Flatté, D. J. Scalapino, *ibid.* **71**, 3363 (1993).
8. M. I. Salkola, A. V. Balatsky, D. J. Scalapino, *ibid.* **77**, 1841 (1996).
9. A. P. Kampf and T. P. Devereaux, *Phys. Rev. B* **56**, 2360 (1997).
10. M. E. Flatté and J. M. Byers, *ibid.*, p. 11213.
11. _____, *Phys. Rev. Lett.* **80**, 4546 (1998).
12. M. I. Salkola and J. R. Schrieffer, *Phys. Rev. B* **58**, R5952 (1998).
13. P. A. Lee, *Phys. Rev. Lett.* **71**, 1887 (1993).
14. A. V. Balatsky, A. Rosengren, B. L. Altshuler, *ibid.* **73**, 720 (1994).
15. M. Franz, C. Kallin, A. J. Berlinsky, *Phys. Rev. B* **54**, R6897 (1996).
16. R. Joynt, *J. Low Temp. Phys.* **109**, 811 (1997).
17. K. Ziegler, M. H. Hettler, P. J. Hirschfeld, *Phys. Rev. Lett.* **77**, 3013 (1996).
18. A. Yazdani, B. A. Jones, C. P. Lutz, M. F. Crommie, D. M. Eigler, *Science* **275**, 1767 (1997).
19. H. L. Edwards, D. J. Derro, A. L. Barr, J. T. Markert, A. L. de Lozanne, *Phys. Rev. Lett.* **75**, 1387 (1995).
20. S. H. Pan, E. W. Hudson, J. C. Davis, *Rev. Sci. Instrum.* **70**, 1459 (1999).
21. For an introduction to STM, see C. J. Chen, *Introduction to Scanning Tunneling Microscopy* (Oxford Univ. Press, Oxford, 1993).
22. No difference was observed between W and PtIr tips. In both cases, the chemical identity of the last atom on the tip is unknown.
23. D. B. Mitzi, L. W. Lombardo, A. Kapitulnik, S. S. Laderman, R. D. Jacowitz, *Phys. Rev. B* **41**, 6564 (1990).
24. S. H. Pan, E. W. Hudson, J. Ma, J. C. Davis, *Appl. Phys. Lett.* **73**, 58 (1998).
25. M. D. Kirk *et al.*, *Science* **242**, 1673 (1988).
26. Y. Gao, P. Lee, P. Coppens, M. A. Subramanian, A. W. Sleight, *ibid.* **241**, 954 (1988).
27. The value $\Delta$, defined for this purpose as half the distance between the two coherent quasi-particle peaks, varies from 25 to 45 mV over the observed surface, with a typical value of $\Delta_0 = 32$ mV.
28. A. Pomar, M. V. Ramallo, J. Mosqueira, C. Torrón, F. Vidal, *Phys. Rev B* **54**, 7470 (1996).
29. R. Movshovich *et al.*, *Phys. Rev. Lett.* **80**, 1968 (1998).
30. S. F. Lee *et al.*, *ibid.* **77**, 735 (1996).
31. R. Mallozzi, J. Corson, J. Orenstein, J. N. Eckstein, I. Bozovic, *J. Phys. Chem. Solids* **59**, 2095 (1998).
32. A. Yazdani, C. M. Howald, C. P. Lutz, A. Kapitulnik, D. M. Eigler, *Phys. Rev. Lett.*, in press; A. Yazdani *et al.*, http://xxx.lanl.gov/abs/cond-mat/9906001.



33. We acknowledge and thank A. Balatsky, M. Flatté, M. Franz, A. de Lozanne, K. Moler, J. Orenstein, R. E. Packard, and D. J. Scalapino for helpful conversations. Funded by NSF under grants DMR-9458015 and DMR-9623842, by the D. & L. Packard Foundation, and by the U.S. Department of Energy.

19 March 1999; accepted 19 May 1999


# High $H_2$ Uptake by Alkali-Doped Carbon Nanotubes Under Ambient Pressure and Moderate Temperatures


**P. Chen, X. Wu, J. Lin,* K. L. Tan**



**Lithium- or potassium-doped carbon nanotubes can absorb ~20 or ~14 weight percent of hydrogen at moderate (200° to 400°C) or room temperatures, respectively, under ambient pressure. These values are greater than those of metal hydride and cryoadsorption systems. The hydrogen stored in the lithium- or potassium-doped carbon nanotubes can be released at higher temperatures, and the sorption-desorption cycle can be repeated with little decrease in the sorption capacity. The high hydrogen-uptake capacity of these systems may be derived from the special open-edged, layered structure of the carbon nanotubes made from methane, as well as the catalytic effect of alkali metals.**


Hydrogen has been recognized as an ideal energy carrier, but to make it truly useful, end-user $H_2$ storage must be improved. In particular, high storage capacity is desirable when $H_2$ is used as the energy carrier in high-energy density rechargeable batteries and in $H_2/O_2$ fuel cells. For these applications, metal hydridation is the existing method above room temperatures and below 20 to 40 atm of pressure, but these materials are heavy and expensive (*1*, *2*). Cryoadsorption, in which activated carbon is often used as a sorbent, shows its advantages in the moderate size and weight of carbon, but suffers from the severe conditions (liquid nitrogen temperatures and 20 atm of pressure) required to hold the physically adsorbed $H_2$ (*3*, *4*). In any case, the $H_2$ uptake by these systems is less than 6 weight % (Table 1), far lower than that of gasoline or diesel (17.3 weight %). More recently, carbon nanotubes were reported to be a more effective material for $H_2$ uptake. Dollin *et al.* found that single wall carbon nanotube (SWNT) soots could absorb about 5 to 10 weight % of $H_2$ at 133 K and 300 torr (*5*). Chambers *et al.* observed that at 120 atm and room temperature, graphite nanofibers with herringbone structure could store 67 weight % of $H_2$ (*6*). Ye *et al.* used high-purity SWNT and obtained 8.25 weight % of $H_2$ adsorption at 80 K and 100 atm (*7*). All the above $H_2$-uptake systems require high pressure or subambient temperatures, or both. Here we introduce a $H_2$ storage system that uses alkali metal–doped carbon nanotubes (CNTs) as sorbents and operates at ambient pressure and moderate temperatures. The $H_2$ uptake can achieve 20 weight % for Li-doped CNT at 653 K, or 14 weight % for K-doped CNT at room temperature. These values correspond to ~160 (for Li-doped CNT) or 112 kg of $H_2/m^3$ (for K-doped CNT), respectively, and are comparable to those of gasoline and diesel.

The CNTs used in this study were made from catalytic decomposition of $CH_4$ (*8*). After purification, almost all of the catalyst particles were removed. More than 90% of the product was in the form of multiwalled CNTs, and 70% was in the diameter range of 25 to 35 nm. The structure of a CNT is formed by the piling up of graphene sheets in the shape of circular cones with a hollow center. The doping of Li and K to the CNT was carried out by solid-state reactions between CNT and Li- or K-containing compounds, such as carbonates or nitrates. For comparison, Li- and K-doped graphite were prepared by the same procedures. The graphite sample was obtained from Merck with an average diameter of 50 μm. The specific surface area of CNT and graphite is 130 and 8.6 $m^2/g$, respectively. The Li/C and K/C ratio of these alkali-doped carbon materials was about 1/15 as measured by x-ray photoelectron spectroscopy. The density of Li-doped carbon materials was ~0.9 $g/cm^3$ for CNT and ~2.0 $g/cm^3$ for graphite. Hydrogen


Physics Department, National University of Singapore, 10 Kent Ridge Crescent, Singapore 119260.

*To whom correspondence should be addressed.